Janus two-dimensional transition metal dichalcogenide oxides: First-principles investigation of WXO monolayers with X = S, Se, and Te

M. Jahangirzadeh Varjovi,[1] M. Yagmurcukardes,[2,3,4] F. M. Peeters,[2,3] and E. Durgun[1,*]

[1]*UNAM—National Nanotechnology Research Center and Institute of Materials Science and Nanotechnology, Bilkent University, Ankara 06800, Turkey*

[2]*Department of Physics, University of Antwerp, Groenenborgerlaan 171, B-2020 Antwerp, Belgium*

[3]*NANOlab Center of Excellence, Groenenborgerlaan 171, B-2020 Antwerp, Belgium*

[4]*Department of Photonics, Izmir Institute of Technology, 35430 Izmir, Turkey*

(Received 29 March 2021; revised 16 May 2021; accepted 17 May 2021; published 26 May 2021)

Structural symmetry breaking in two-dimensional materials can lead to superior physical properties and introduce an additional degree of piezoelectricity. In the present paper, we propose three structural phases (1H, 1T, and 1T') of Janus WXO (X = S, Se, and Te) monolayers and investigate their vibrational, thermal, elastic, piezoelectric, and electronic properties by using first-principles methods. Phonon spectra analysis reveals that while the 1H phase is dynamically stable, the 1T phase exhibits imaginary frequencies and transforms to the distorted 1T' phase. *Ab initio* molecular dynamics simulations confirm that 1H- and 1T'-WXO monolayers are thermally stable even at high temperatures without any significant structural deformations. Different from binary systems, additional Raman active modes appear upon the formation of Janus monolayers. Although the mechanical properties of 1H-WXO are found to be isotropic, they are orientation dependent for 1T'-WXO. It is also shown that 1H-WXO monolayers are indirect band-gap semiconductors and the band gap narrows down the chalcogen group. Except 1T'-WSO, 1T'-WXO monolayers have a narrow band gap correlated with the Peierls distortion. The effect of spin-orbit coupling on the band structure is also examined for both phases and the alteration in the band gap is estimated. The versatile mechanical and electronic properties of Janus WXO monolayers together with their large piezoelectric response imply that these systems are interesting for several nanoelectronic applications.

DOI: 10.1103/PhysRevB.103.195438

I. INTRODUCTION

The successful isolation of single-layer graphene and unveiling its novel properties [1] has stimulated the research on ultrathin two-dimensional (2D) materials. Within the 2D dynasty, transition metal dichalcogenides (TMDs) and transition metal oxides (TMOs) (with the general chemical formula MX_2 where M refers to a transition metal atom and X is a chalcogen atom) [2–6] have obtained considerable attention due to their stability and remarkable electronic properties ranging from semiconducting and metallic to superconducting [7–9]. This makes them of interest for both fundamental studies and high technological applications [10,11]. One of the prominent members of this family is WX_2 and it possesses three possible structural phases, in which W atoms are sandwiched between two layers of X atoms. Depending on the coordination arrangement of W and X atoms, monolayer WX_2 can be formed either in the honeycomb [12] (1H-WX_2, trigonal prismatic structure), centered honeycomb [5] (1T-WX_2, octahedral), or distorted [13] (1T'-WX_2, distorted octahedral) structures. 1H-WX_2 is the most stable configuration under ambient conditions and can be obtained by mechanical exfoliation from its bulk counterpart or can be synthesized via chemical vapor deposition [14–16]. The metallic 1T-WX_2 has been shown to be unstable [17,18], and transforms to 1T'-WX_2 due to the Peierls distortion, which also results in the formation of charge density waves [19,20]. 2D WS_2 crystals exhibit superior optical properties [21,22] and larger spin-orbit coupling (SOC) [23] than 2D MoS_2, which makes them interesting for optoelectronic and spintronic applications. Similar to WS_2, the WSe_2 monolayer in the 1H phase is a semiconductor with a direct band gap of ∼1.6 eV and carrier mobility ∼250 cm^2/V [24]. In addition, the monolayer of WSe_2 has been reported to be the first TMD presenting a p-type conductive behavior with a large work function (with palladium contacts) [24,25]. Recently, it has been shown that the 1T'-WTe_2 monolayer is a type-II Weyl semimetal with a large nonsaturating magnetoresistance [26,27]. Accordingly, the outstanding physical properties of WX_2 monolayers such as high carrier mobility at room temperature [24] and tunable electronic properties (by an external field or by strain engineering) [28,29] make them suitable for many applications, including energy conversion and hydrogen production [30].

In addition to binary systems, several 2D Janus TMDs have been fabricated recently, following the realization of MoSSe monolayers [31,32], including WSSe [33,34] and PtSSe [35]. In Janus TMDs, chalcogen atoms in one of the layers are fully replaced with another chalcogen atom (e.g., S with Se) which results in structural symmetry breaking along the vertical direction. This broken out-of-plane symmetry and the additional degree of freedom lead to distinct features, including

*durgun@unam.bilkent.edu.tr

the enhancement of the piezoelectric constants, especially in the out-of-plane direction [36,37]. Together with experimental progress, various 2D Janus systems have been predicted and characterized by *ab initio* methods [36,38–42]. For instance, the electronic, mechanical, and piezoelectric properties of Janus MoSTe monolayers in $1H$- and $1T'$-phases have been investigated and it was found that the out-of-plane piezoelectric coefficient is nonzero [43]. In another study, it was reported that the WSTe monolayer has large Rahsba spin splitting parameters which are tunable by in-plane strain [44]. The energy difference between the $1H$ and $1T'$ phases of Janus WSeTe monolayers are small, allowing for an electrostatically driven reversible phases transition between the stable phases plausible [45].

Like the Janus systems based on TMDs, the monolayer of MoSO was also found to be dynamically stable and possess a strong out-of-plane piezoelectricity which originates from the large charge difference between the S and O surfaces [46]. As an oxygen ion has a typical character, 2D TMOs have notable features and can be used in variety of applications [47–50]. In that sense, to oxidize the surface of 2D WX_2 crystals, several approaches such as oxygen plasma and UV/ozone treatment have been proposed [51,52]. Additionally, a new member of TMOs [53], tungsten oxysulfide [54] (WO_yS_x) has been discovered and shown to be a highly efficient catalyst in hydrogen evolution reactions. Despite the various experimental and theoretical studies on Janus WXX' systems, the formation of Janus WXO monolayers based on oxygenation of WX_2 have not been realized yet.

In this paper, inspired by the already realized 2D ternary TMDs and TMOs, and the novel properties of binary WX_2 systems, we design and investigate the structural, vibrational, thermal, mechanical, piezoelectric, and electronic properties of $1H$, $1T$, and $1T'$ phases of WXO (X = S, Se, and Te) Janus monolayers by first-principle methods. The paper is organized as follows: The computational methodology is described in Sec. II. In Sec. III, first the ground-state structures of three common phases of WXO monolayers are obtained and their relevant structural parameters and cohesive energies are reported. Then the dynamical stability of the monolayers is systematically investigated by the analysis of their phonon spectrum and using *ab initio* molecular dynamics (AIMD) simulations. Next, vibrational, mechanical, piezoelectric, and electronic properties of WXO Janus monolayers are examined. Our conclusions are presented in Sec. IV.

II. METHODOLOGY

First-principles calculations were carried out in the framework of density functional theory [55,56] as implemented in the Vienna Ab initio Simulation Package [57–60]. The projector augmented wave [61] method was used to portray the potentials of W, O, S, Se, and Te elements. The exchange-correlation potential was treated by the generalized gradient approximation (GGA) within the Perdew-Burke-Ernzerhof (PBE) form [62]. A plane-wave basis set with the kinetic energy cutoff $\hbar^2|\mathbf{k}+\mathbf{G}|^2/2m = 520$ eV was used for all calculations. The convergence value for electronic relaxation between the sequential steps in the total energy calculations is taken to be 10^{-5} eV. For the optimization of the ionic positions and lattice constants, the conjugate gradient method was employed until the Hellmann-Feynman forces on each atom were less than 0.01 eV/Å. To prevent any artificial interaction between neighboring images, a vacuum spacing of ∼20 Å was set in nonperiodic direction. The SOC was taken into account during the calculation of electronic band structures. To obtain more accurate electronic band gaps, the hybrid functional of Heyd-Scuseria Ernzerhorf (HSE06) with SOC was adopted and compared with GGA-PBE results [63,64]. The screening length of HSE06 and the mixing rate of the Hartree-Fock exchange potential were taken as $\lambda = 0.2$ Å^{-1} and 0.25, respectively. The Brillouin zones of $1H$-, $1T$-, and $1T'$-WXO were sampled by using Γ-centered $24\times24\times1$, $24\times24\times1$, and $24\times16\times1$ uniform k-point meshes, respectively [65]. The phonon spectrum analyses were performed by $5\times5\times1$ supercells for $1H$, $1T$, and $6\times4\times1$ supercells for $1T'$ structures using the small-displacement method as implemented in PHONOPY [66].

The first-order off-resonant Raman spectrum of each phonon mode was obtained by calculating the macroscopic dielectric tensor using the small difference method at the Γ point [67]. To obtain the piezoelectric stress coefficients, the density functional perturbation theory method with a sufficiently large k-point grid and cutoff energy of 700 eV was used. To examine the dynamical stability of the optimized structures, AIMD calculations were performed by implementing a microcanonical ensemble simulation at constant temperatures (300 K and 600 K) with a total simulation time of 3 ps. To understand the bond characteristics of the structures, charge transfer calculations between the atoms are conducted by employing the Bader method [68].

III. RESULTS AND DISCUSSION

A. Atomic structure and energetics

Prior to the design of Janus WXO (X = S, Se, Te) systems, we start with investigating the structural properties of the three common phases of binary WX_2 monolayers. The geometry of $1H$, $1T$, and $1T'$ belong to the D_{3h}, D_{3d}, and C^2_{2h} space groups, respectively. The calculated structural properties are summarized in Table S1, Supplemental Material [69], which are in good agreement with previous studies [29,70]. Once the binary WX_2 systems are obtained, Janus WXO monolayers are constructed by substituting X atoms of the top layer by O atoms. Top and side views of $1H$-, $1T$-, and $1T'$-WXO are illustrated in Figs. 1(a) and 1(b). Notice that the lattice constants (**a** and **b**) of $1H$- and $1T$-WXO monolayers increase down the chalcogen group. The bond length between W and X atoms (d_{W-X}) and the thickness of the crystals (h) follows a similar trend as d_{W-X} elongates and h thickens with an increasing atomic radius of X atoms. Not surprisingly, the bond length between W and O atoms (d_{W-O}) remains almost the same for all the systems. Our results also indicate that the lattice parameter of WXO is between those of WX_2 and WO_2 monolayers. Therefore, up and down sides of these structures undergo different types of induced biaxial strain (i.e., the O side experiences tensile strain whereas the X side is under compressive strain). Similar to binary counterparts, $1T$-WXO transforms into a $1T'$ phase due to Peierls distortion. This distorted phase has been found to be energetically

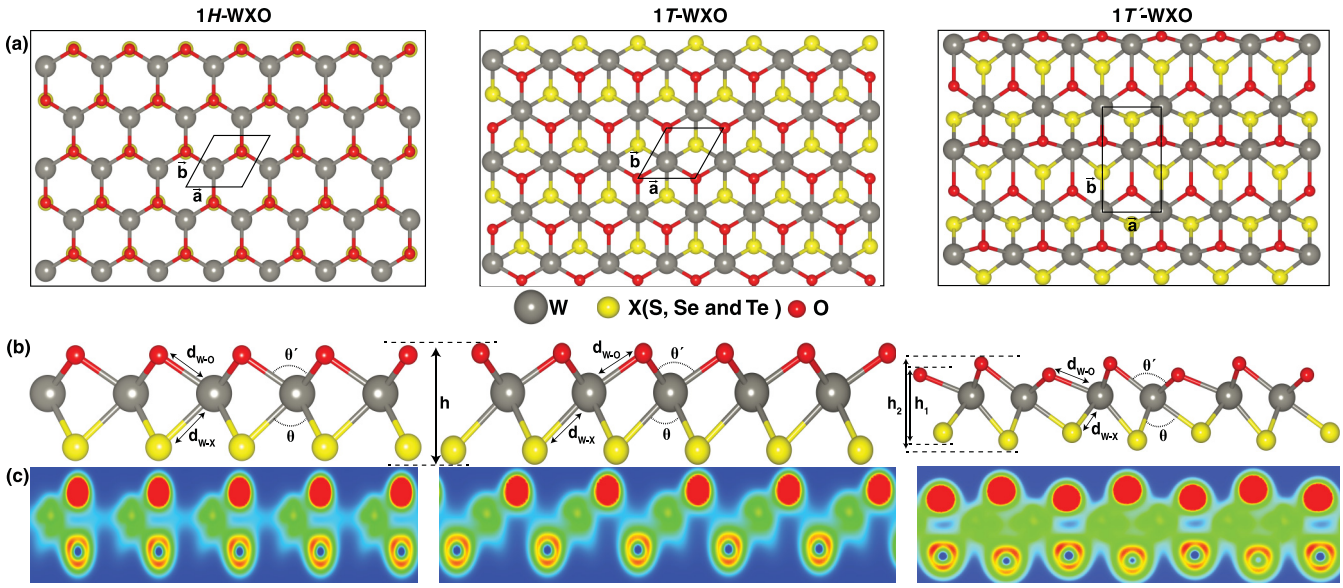

FIG. 1. (a) Top, (b) side views of the structures, and (c) total charge distribution profile of 1H-, 1T-, and 1T'-WXO monolayers. A color scheme with linear scaling from blue (lowest) to red (highest) is used for charge profile. The relevant structural parameters are labeled. In (a), the unit cell is shown by the black polygon.

more favorable than the 1T phase in various systems including $RuSe_2$ [71], ReS_2 [72], MoX_2 [17,73,74], and WX_2 [17,26,74] monolayers. To model 1T'-WXO monolayers, first a 1×2 supercell is constructed and then the same design principles are applied. As summarized in Table I, similar to other phases, **a**, **b**, d_{W-X}, h of the 1T'-WXO structures increase down the chalcogen group. It should be noted that due to the broken symmetry, the bond lengths are not uniform and, additionally, two thicknesses (h_1 and h_2) are labeled [Fig. 1(b)].

To analyze the strength of the binding between the atoms, the cohesive energy per atom (E_C) of the WXO structures is calculated with the following formula:

$$E_C = \frac{[N_W E_T(\mathrm{W}) + N_X E_T(X) + N_O E_T(\mathrm{O})] - [E_T(\mathrm{W}XO)]}{[N_W + N_X + N_O]} \quad (1)$$

where E_T(W), $E_T(X)$, and E_T(O) are the single atom energies of W, X, and O elements, respectively; E_T(WXO) corresponds to the total energy of the WXO monolayer; N_W, N_X, and N_O are the total number of W, X, and O elements in the unit cell. All calculated E_C's, which are summarized in Table I, are positive and relatively large, indicating strong binding between the constituent atoms. The covalent character of the bonds is also shown in Fig. 1(c). Similar to the binary counterparts, E_C decreases down the chalcogen group in parallel with the variation of **a** (or **b**) and d_{W-X}. The highest E_C's are obtained for the 1H phase, except WTeO, where 1H and 1T' phases have almost the same energy. As expected, E_C's of 1T' phase are larger than those of the 1T phase due to the energy lowering as a consequence of the Peierls distortion. According to the Bader charge analysis, while the charge depletion from W to O atoms [$\Delta\rho_{(W-O)}$] remains almost

TABLE I. For monolayers of 1H-, 1T-, and 1T'-WXO, we present the optimized lattice constants, **a** and **b**; atomic bond lengths, d_{W-X} and d_{W-O}; thickness, h; bond angle between X-W-X, θ and O-W-O, θ'; average charge transfer from W to X, $\Delta\rho_{(W-X)}$ and W to O, $\Delta\rho_{(W-O)}$; and the cohesive energy per atom, E_C.

Crystal phase	a (Å)	b (Å)	d_{W-X} (Å)	d_{W-O} (Å)	h (Å)	θ (deg)	θ' (deg)	$\Delta\rho_{(W-X)}$ (e^-)	$\Delta\rho_{(W-O)}$ (e^-)	E_C (eV/atom)
1H-WSO	3.01	3.01	2.38	2.09	2.80	78.2	91.8	0.59	0.97	6.27
1H-WSeO	3.07	3.07	2.50	2.10	2.91	75.5	93.6	0.42	0.98	5.87
1H-WTeO	3.19	3.19	2.69	2.13	3.04	72.5	96.8	0.22	1.01	5.36
1T-WSO	3.05	3.05	2.41	2.08	2.75	78.6	94.0	0.65	1.01	5.97
1T-WSeO	3.09	3.09	2.54	2.09	2.90	74.8	95.4	0.47	1.01	5.63
1T-WTeO	3.21	3.21	2.74	2.10	3.02	71.4	99.3	0.27	1.03	5.22
1T'-WSO	3.06	5.42	2.36/2.38 2.43/2.45	2.03/2.06 2.24/2.29	2.30/3.05	69.2/79.4 82.1/93.0	77.9/88.2 98.1/108.4	0.61	0.99	6.08
1T'-WSeO	3.09	5.69	2.49/2.53 2.57/2.58	2.02/2.03 2.29/2.63	2.38/3.23	65.0/77.7 81.5/94.8	77.1/88.3 97.7/108.5	0.43	0.98	5.73
1T'-WTeO	3.17	6.43	2.69/2.76 2.78/2.85	1.97/2.06 2.16/3.57	2.39/3.41	60.1/78.3 86.5/105.5	80.4/92.4 93.5/104.3	0.26	0.98	5.38

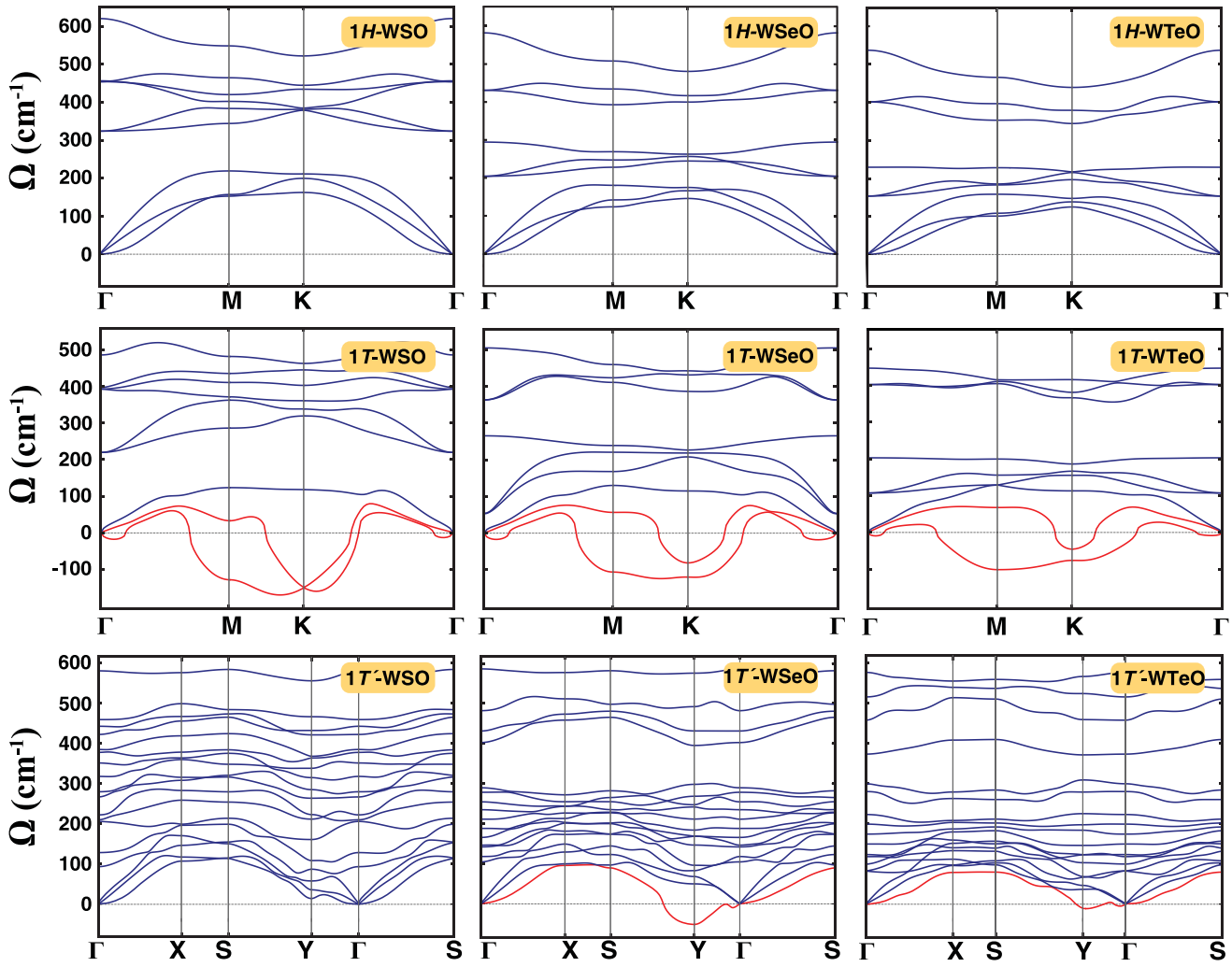

FIG. 2. Phonon spectra of Janus 1H-, 1T-, and 1T'-WXO monolayers. Imaginary frequencies are indicated by red color.

constant in all the structures, the average charge transfer between X and W atoms $[\Delta\rho_{(W-X)}]$ decreases down the chalcogen group associated with the decreasing electronegativity difference between W and X atoms ($\Delta\chi$). As $\Delta\rho_{(W-X)}$ strongly depends on $\Delta\chi$, the variation over the different structural phases is not significant. The change of E_C with the X atom is in line with the variation of $\Delta\rho_{(W-X)}$. Additionally, E_C of WXO Janus crystals are in between those of the WX_2 and WO_2 binary constituents. In other words, oxygenation of WX_2 increases the cohesive energy of the system.

B. Dynamical stability

To examine the dynamical stability of the proposed structures, vibrational frequency analysis is performed, and corresponding phonon band diagrams are represented in Fig. 2. All phonon spectra of 1H-WXO are found to be free from any imaginary frequencies over the whole BZ, indicating structural stability. It is seen that the phonon band gap between acoustical and optical modes becomes narrower, and the frequencies of phonon modes (including the maximum phonon frequency, ω_{max}) gradually decrease from 1H-WSO to 1H-WTeO as a result of increasing the weight the X atom. A careful analysis of the force constant matrices reveals that this reduction is not only due to the increased mass of the X atoms but also to the weakening of interatomic bonding between the atoms. However, the phonon spectra of 1T-WXO monolayers have imaginary frequencies labeled with solid red lines in Fig. 2. These soft acoustic modes indicate that metallic 1T-WXO monolayers are prone to instability and transform to 1T' phase due to Peierls distortion. These imaginary frequencies in the phonon spectrum are removed in the 1T' phase. (Notice that 1T'-WSeO and 1T'-WTeO possess small imaginary frequencies around the Y high symmetry point which can be correlated with charge density waves [75]). They disappear if we allow for charge density waves. Based on 1×2 reconstruction, phonon spectra of the Janus 1T'-WXO crystals have eighteen discrete phonon modes composed of three acoustical and 15 optical branches. All these modes are nondegenerate because of the broken structural symmetry.

To further investigate the structural stability of the WXO monolayers at high temperatures, AIMD simulations are performed. To remove the size constraint, the same supercell sizes that were considered in the phonon spectrum analysis are used. The AIMD simulations are carried out at 300 K and 600 K for a total simulation time of 3 ps. Apart from small

fluctuations of the atoms around their equilibrium positions, the crystalline morphology of $1H$ and $1T'$ phases are preserved, confirming the dynamical stability of these systems at and above ambient temperature. The final snapshots of the resulting atomic structures taken at 300 K and 600 K are shown in Figs. S1 and S2, Supplemental Material [69], respectively. It should be noted that even Janus WXO monolayers are structurally stable, their freestanding form can be curled due to the stress on the outer layers [76,77].

C. Vibrational properties

Raman spectroscopy analysis and the vibrational characteristics of phonon modes at the Γ point are useful techniques to investigate the lattice symmetries and crystallographic phase-dependent properties of a material. $1H$-WX_2 monolayers belong to the D_{3h} space group and consist of three atomic sublayers (X-W-X), which are held together via covalent bonding. By replacing one of the chalcogenide layers with O atoms, the out-of-plane symmetry is broken and additional Raman active modes appear. $1H$-WXO monolayers have C_{3v} symmetry, and the corresponding irreducible representation for phonon modes in their spectrum is given by $\Gamma = 2A_1 + 2E$, in which the A_1 and E modes are both IR and Raman active. All nondegenerate A_1 eigenmodes are attributed to the vibration along the z direction, whereas E phonon modes represent the doubly degenerate in-plane vibrations. Therefore, in total, there are four Raman active modes in the $1H$-WXO monolayers. As can be seen from Fig. 3(a), in $1H$-WXO, the Raman activity of $A_1^{(W-X)}$ is very robust, which originates from the relatively higher contribution of the out-of-plane macroscopic dielectric constants to the Raman tensors. For the sake of comparison, the calculated Raman spectra of $1H$-WX_2 monolayers are also depicted. Similar to the experimental [33] and simulated [78] Raman spectra of WSSe monolayers, the $A_1^{(W-X)}$ mode is the most prominent peak in the $1H$-WXO monolayers. The frequencies of the $A_1^{(W-X)}$ mode in the $1H$ phases are 456 cm^{-1}, 297 cm^{-1}, and 224 cm^{-1} for WSO, WSeO, and WTeO monolayers, respectively. As shown in Fig. 3(b), there are four distinct eigenmodes present in the optical spectrum of the $1H$ Janus structures. In the lower energy E phonon mode, the X atom moves in opposite in-plane directions of the W-O couple, whereas in the higher frequency E mode, the O atoms and the W-X pairs vibrate in the opposite in-plane direction of each other and the magnitude of the O eigenvectors are significantly larger than those of W-X. The $A_1^{(W-X)}$ mode arises from the out-of-plane vibration of X and W atoms in the opposite directions. Unlike WX_2 systems, the center of mass in the Janus $1H$-WXO structures are not at the W layer; thus the center of vibration is in between the W-X bonds for $A_1^{(W-X)}$ vibrational mode. The $A_1^{(W-O)}$ phonon mode originates from the strong bond stretching of W-O atoms. In this mode, W and O atoms vibrate in the z direction against each other and the displacement of the O atoms is more significant.

As mentioned, the space group of the $1T'$-WX_2 monolayers belongs to C_{2h}^2. Our analyses shows that the irreducible representation for the optical spectrum in the $1T'$-WX_2 structure can be described by $\Gamma = 2A_u + 4B_u + 6A_g + 3B_g$, in which six optical modes (A_u and B_u) and the other nine modes (A_g and B_g) are IR and Raman active, respectively. Due to the broken symmetry along the z direction by replacing O atoms with the chalcogenide atoms in the $1T'$-WX_2 structures, the symmetry of the new structures ($1T'$-WXO) is described by the C_{2v}^7 space group. Similar to its binary counterpart, the $1T'$-WXO monolayer consists of six atoms within the primitive cell, resulting in 15 optical branches. All optical phonon modes in the $1T'$-WXO structures are nondegenerate and Raman active. The calculated Raman activity of $1T'$-WXO crystals are shown in Fig. 3(c). Notice from Figs. 3(a) and 3(c) that two different structural phases of the WXO monolayers exhibit completely different Raman spectra. The prominent peaks in the Raman spectra of $1T'$-WSO are labeled with numbers, and the vibrational motion of the corresponding peaks are illustrated in Fig. 3(d). The I and II peaks are mostly dominated by in-plane and out-of-plane vibration of W atoms, respectively. For the Raman modes labeled as III and IV, all atoms in the primitive cell vibrate along different directions. The V peak mode is attributed to the vibration of O and S atoms in the out-of-plane direction. The peak VI (with the frequency of 377 cm^{-1}) corresponds with a dominant in-plane vibration of O atom in the unit cell. For peaks VII and VIII, the out-of-plane vibration of the outer S atoms against O atoms is more dominant, while in the remaining peaks the strong out-of-plane vibration of O atoms is the reason for the robust peaks in the Raman activity diagram. It can be concluded that the Raman spectra of the $1T'$ structures are significantly different from those of $1H$ phase.

D. Thermal properties

Having obtained the phonon spectra, we also investigated the isovolume heat capacity (C_V) of WXO monolayers, which is related to the ability of a material to store heat for a given temperature range. It is known that the lattice vibrations in ultrathin materials give the dominate contribution to the specific heat capacity, while the role of the free conduction electrons is negligible [79,80]. Figure 4 presents C_V of $1H$- and $1T'$-WXO structures up to 600 K, at which structural stability is still maintained. Our results reveal that, similar to bulk systems, C_V increases with temperature and approaches the classical Dulong-Petit limit, i.e., $3Nk_B$, where N is the number of atoms in the unit cell, and k_B is the Boltzmann constant. Up to room temperature, C_V moderately increases down the chalcogen group for both phases, and this can be correlated with the shift of the optical phonon modes with X [81]. C_V varies more rapidly for the high-frequency optical branches than for the low-frequency acoustic branches at low temperatures. Moreover, it has been reported that the C_V of 2D materials at low temperatures scales with $T^{2/n}$ ($n > 0$). n is obtained from the following relation: $\omega = q^n$, where ω is the frequency of vibration and q is the wave vector of the acoustical phonon modes around the Γ point [79,80]. Accordingly, n is estimated as 1.01–1.05 and 1.12–1.15 for $1H$ and $1T'$ phases, respectively. Accordingly, while C_V of $1H$-WXO varies with T^2, it increases with $T^{1.75}$ for $1T'$-WXO. In addition, with this analysis, it is found that the main contribution to the C_V arises from in-plane LA-TA modes, and out-of-plane ZA mode for $1H$-WSO and $1T'$-WSO monolayers, respectively.

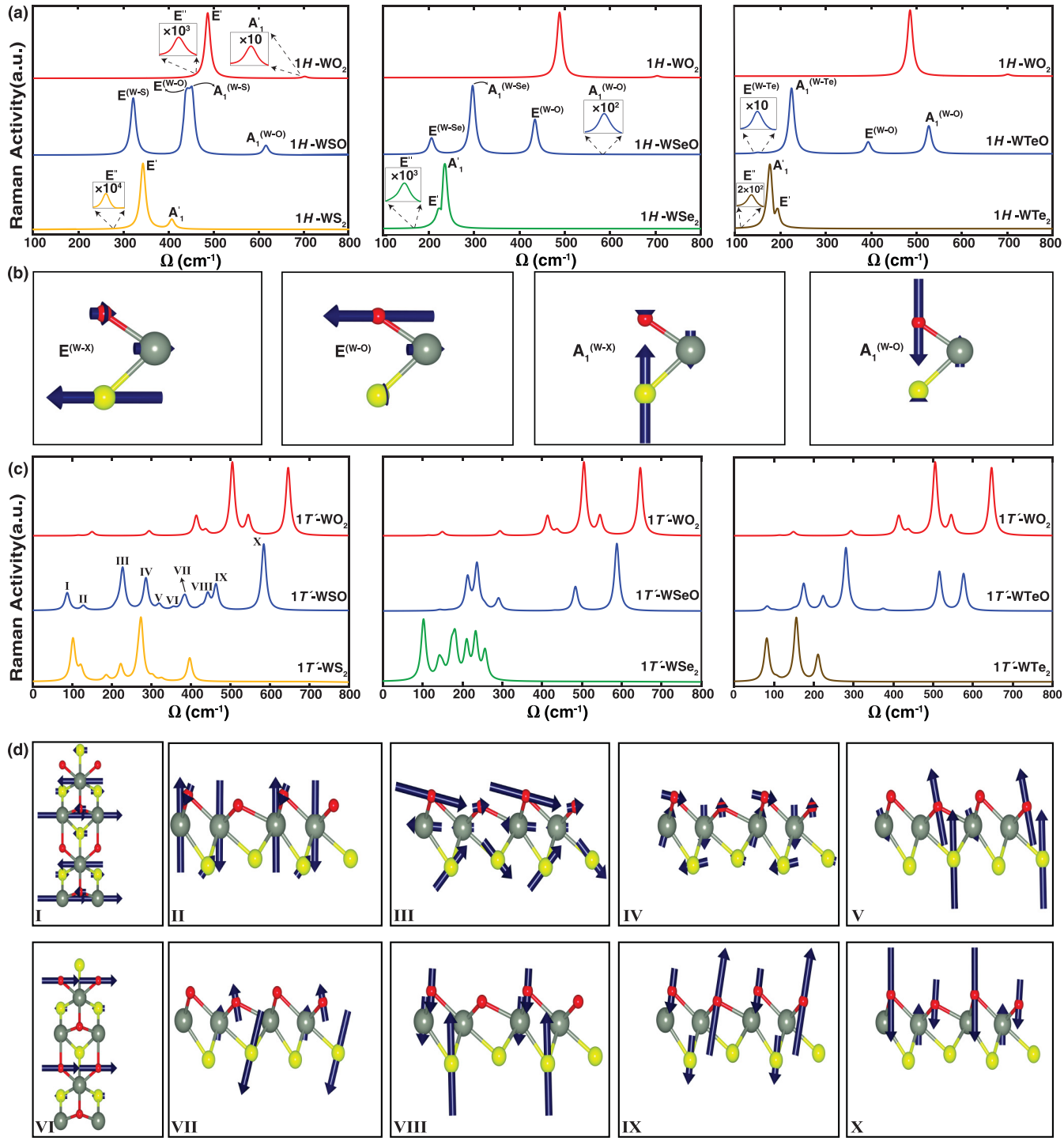

FIG. 3. The normalized Raman activity spectra [(a), (c)] and corresponding atomic displacement [(b), (d)] of the Raman activity modes of $1H$ [(a), (b)] and $1T'$ [(c), (d)] phases of WX_2 and WXO monolayers.

E. Linear-elastic and piezoelectric properties

The mechanical response of 2D materials in the elastic regime can be represented by two linear-elastic constants: the in-plane stiffness (C) and the Poisson ratio (ν). In the present study, these constants are obtained from the elastic-strain tensor elements, c_{ij}, and their values for two specific orientations, namely, zigzag (zz) and armchair (ac), can be calculated using the relations below:

$$C_{zz} = \frac{\left(c_{11}c_{22} - c_{12}^2\right)}{c_{22}}, \quad C_{ac} = \frac{\left(c_{11}c_{22} - c_{12}^2\right)}{c_{11}}, \tag{2}$$

and, similarly, the Poisson's ratio can be written as

$$\nu_{zz} = \frac{c_{12}}{c_{22}}, \quad \nu_{ac} = \frac{c_{12}}{c_{11}} \tag{3}$$

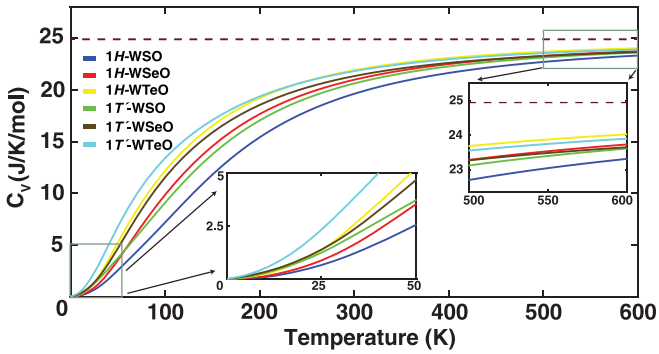

FIG. 4. Variation of isovolume heat capacity (C_V) for the 1H- and 1T'-WXO monolayers with temperature. The low and high temperature limits are shown as insets.

The in-plane stiffness, C, is the measure of the rigidity of a material in the 2D limit analogous to Young's modulus in 3D structures. C is isotropic for 1H − WXO and has the same value along all orientations. In Table II, C_{zz} and C_{ac}, are given for the sake of comparison with the T' phase. Notice that C decreases with increasing atomic radius of the X atoms along with elongation of d_{W-X}. The calculated C's are 182, 169, and 150 N/m for monolayers of 1H-WSO, 1H-WSeO, and 1H-WTeO, respectively. In contrast, 1T'-WXO structures are shown to possess in-plane anisotropy arising from the formation of W-W chains in the crystal. It was already observed in MTe$_2$ (M = Mo or W) layered crystals that due to the large atomic radius of Te atoms, Mo or W atoms tend to get closer and form M-M chains which lead to in-plane anisotropy [82]. The anisotropy becomes more evident as the atomic radius difference between the O and X atoms increases. The reason for the increasing anisotropy degree in WSeO and WTeO can be related to the induced surface strains on O and X sites. Therefore, the response of the lattice to the applied external load is different as one of the chalcogen layer of WX_2 is replaced by O. C_{zz} (C_{ac}) are calculated as 130 N/m (128 N/m), 140 N/m (43 N/m), and 89 N/m (27 N/m) for 1T'-WSO, 1T'-WSeO, and 1T'-WTeO, respectively. Apparently, the difference between zigzag and armchair orientations increases down the chalcogen group. Additionally, bond weakening results in a decrease in stiffness. As compared to the stiffness values predicted for other Janus TMDs (ranges between 106–117 N/m for 1H-MoXY and 139-146 N/m for 1H-WXY) [83], 1T'-WTeO is quite softer, especially along the ac orientation. The significant decrease of the stiffness along this direction for 1T'-WSeO and 1T'-WTeO can be attributed to the increasing surface strain on the O site. As the atomic radius of the X atom increases with Se or Te atoms on one side, the perpendicular distance between W-W chains increases, and thus the W-O distance increases also. The increasing W-O distance, therefore, results in the weakening of the stiffness along the W-O direction.

Poisson's ratio (ν) is defined as the negative ratio of the transverse strain to the longitudinal strain and correlates the deformation along the applied stress to the deformation in the vertical direction. Similar to C, ν is also isotropic and has the values 0.27, 0.24, and 0.22 for 1H-WSO, 1H-WSeO, and 1H-WTeO, respectively. As $\nu < 0.33$, 1H-WXO monolayers are brittle according to the Christensen criterion [84], similar to their WX_2 counterparts. The predicted ν values for WS_2, WSe_2, and WTe_2 were reported to be 0.21, 0.26, and 0.34, respectively, and display a different behavior than 1H-WXO due to the presence of O atoms on one side [83]. In the case of 1T'-WXO monolayers, the anisotropy becomes more drastic as the difference in atomic radius of X and O atoms increases. ν_a (ν_b) are estimated as 0.14 (0.13), 0.21 (0.06), and 0.26 (0.08) for 1T'-WSO, 1T'-WSeO, and 1T'-WTeO, respectively. Similar to the 1H-phase, 1T'-WXO monolayers are also brittle and being $\nu_b \sim 0.1$ indicates enhanced covalent bonding character in that direction [84].

Piezoelectricity is described as the generating electric dipole moment as a result of applied external stress (and vice versa) in noncentrobinary structures [85]. Experiments have demonstrated enhanced piezoelectric constants in the 2D limit [86]. For 2D ultrathin materials, the relaxed-ion piezoelectric tensor is given as

$$e_{ij} = e_{ij}^{\mathrm{el}} + e_{ij}^{\mathrm{ion}}, \tag{4}$$

where e_{ij}^{el} and e_{ij}^{ion} represent the electronic and ionic contributions, respectively. e_{ij}'s are related to the piezoelectric strain (d_{ij}) and the elastic stiffness (c_{kj}) tensor elements:

$$e_{ij} = d_{ik} c_{kj}. \tag{5}$$

For the 1H-phase, d_{ij} are given by the relations

$$d_{11} = \frac{e_{11}}{c_{11} - c_{12}}, \quad d_{13} = \frac{e_{13}}{c_{11} + c_{12}}. \tag{6}$$

It should be noted that while e_{13} is zero in 1H-WX_2, broken out-of-plane symmetry adds a degree of freedom to piezoelectricity in 1H-WXO and e_{13} is no longer zero. The e_{11}

TABLE II. The relaxed-ion elastic coefficients, c_{ij}; in-plane stiffness, C; and Poisson's ratio, ν along two orientations, namely, zigzag (zz or a) and armchair (ac or b) for 1H- and 1T'-WXO.

Crystal structure	c_{11} (N/m)	c_{22} (N/m)	c_{12} (N/m)	C_{zz} (N/m)	C_{ac} (N/m)	ν_{zz} (−)	ν_{ac} (−)
1H-WSO	196	196	52	182	182	0.27	0.27
1H-WSeO	179	179	44	169	169	0.24	0.24
1H-WTeO	158	158	34	150	150	0.22	0.22
1T'-WSO	132	130	18	130	128	0.14	0.13
1T'-WSeO	142	44	9	140	43	0.21	0.06
1T'-WTeO	91	28	7	89	27	0.26	0.08

TABLE III. The relaxed-ion piezoelectric stress, e_{ij}, and the corresponding piezoelectric strain coefficients, d_{ij} for the 1H- and 1T'-WXO monolayers. Note that the values for e_{ij} are multiplied by 10^{-10} order.

Crystal phase	e_{11} (C/m)	e_{13} (C/m)	e_{14} (C/m)	e_{21} (C/m)	e_{22} (C/m)	d_{11} (pm/V)	d_{13} (pm/V)	d_{14} (pm/V)	d_{21} (pm/V)	d_{22} (pm/V)
1H-WSO	2.5	1.1	–	–	–	1.8	0.4	–	–	–
1H-WSeO	2.6	1.2	–	–	–	1.9	0.5	–	–	–
1H-WTeO	3.4	1.2	–	–	–	2.8	0.6	–	–	–
1T'-WSO	–	–	13.4	16.1	8.2	–	–	25.8	15.4	3.3
1T'-WSeO	–	–	5.6	19.1	7.4	–	–	12.7	16.3	35.6
1T'-WTeO	–	–	1.3	3.3	1.9	–	–	1.7	5.1	4.6

coefficients are calculated to be 2.5×10^{-10}, 2.6×10^{-10}, and 3.4×10^{-10} C/m for 1H-WSO, 1H-WSeO, and 1H-WTeO crystals, respectively. Besides, the out-of-plane components of the piezoelectric stress tensor are found to be quite significant, 0.4, 0.5, and 0.6 pm/V, which are much larger than those of Janus MoSSe (∼0.1 pm/V) [31]. This is related to the large charge difference on both surfaces arising from the O atoms.

As the structural symmetry changes from 1H to 1T', the number of nonzero piezoelectric tensor elements becomes e_{14}, e_{21}, and e_{22}. As listed in Table III, e_{14} and e_{22} decreases as X atoms change from O to Te. The two coefficients represent the induced dipole moment along $x-y$ and y directions when the external strain is applied along x and y directions (i.e., zz and ac), respectively. Therefore, the decreasing trend indicates a decline in the in-plane dipole moment caused by the charge density difference on X and O atoms.

The related d_{ij} values are calculated by using the following relations:

$$d_{14} = \frac{e_{14}}{c_{44}}, \quad d_{21} = \frac{2e_{21}c_{12} + e_{21}c_{11} + e_{22}c_{11}}{3c_{11}c_{12} + c_{11}^2},$$
$$d_{22} = \frac{e_{21}c_{12} - e_{22}c_{11}}{3c_{22}c_{12} + c_{11}c_{22}}, \tag{7}$$

and found to be one-order larger than those for the isotropic 1H-phase structures. It is important to note that the formation of distorted Janus structures of WXO creates in-plane piezoelectricity, which is absent in binary 1T'-WX_2. Therefore, the creation of out-of-plane asymmetry is important not only for out-of-plane piezoelectricity but also for the in-plane components in the distorted phase of TMDs. Prediction of distorted Janus materials will enrich the family of piezoelectric materials [87].

F. Electronic properties

Lastly, the electronic properties of 1H- and 1T'-WXO monolayers are investigated. The calculated electronic band structures and orbital projected density of states (PDOS) are presented in Fig. 5 and Figs. S2 and S3, Supplemental Material [69], respectively. As summarized in Table S1, Supplemental Material [69] while 1H-WX_2 (X = S, Se, and Te) monolayers are direct band-gap semiconductors, 1H-WO_2 monolayer has an indirect band gap. Therefore, 1H-WXO systems are found to be indirect band-gap semiconductors, as shown in Fig. 5. Direct to indirect band-gap transitions can also be related with the induced strain on the outer layer (i.e., while the O side undergoes tensile strain, the X side experiences a compressive strain). The calculated band gap values at the level of GGA-PBE (E_g^{PBE}) are 1.52, 1.28, and 0.71 eV for 1H-WSO, 1H-WSeO and 1H-WTeO monolayers, respectively. It is noticed that E_g^{PBE} decreases down the group of chalcogen atoms in line with the variation of $\Delta\rho_{(W-X)}$. E_g^{PBE} of 1H-WXO are narrower than those of WX_2 systems but follow the same trend. The inclusion of SOC decreases the band gap values ($E_g^{\mathrm{PBE-SOC}}$), and expectedly the impact is more prominent for 1H-WTeO, being Te is the heaviest element among the chalcogens. Similar trends with wider band gap values ($E_g^{\mathrm{HSE-SOC}}$) are obtained when calculations are repeated with hybrid functionals with the inclusion of SOC. As can be seen from Table S1, Supplemental Material [69], 1T'-WX_2 monolayers other than 1T'-WO_2 are semiconductors, which is correlated with the Peierls distortion [88,89]. The metallic T-phase is prone to instability and transforms to T'-phase, and results in a metal to semiconductor transition. Similar results are also obtained for 1T'-WXO. As discussed above, 1T-WXO monolayers are unstable, and a phase transition from 1T to 1T' is realized. As 1T'-WO_2 is a semimetal, the band-gap variation of 1T'-WXO does not follow a clear trend. As shown in Fig. 5, while 1T'-WXO is a semimetal, E_g^{PBE} of 1T'-WSeO and 1T'-WTeO are 0.25 and 0.41 eV, respectively. The increase in band gap is correlated with the structural deformation (Table I). Akin to the 1H phase, the inclusion of SOC lowers the band gap ($E_g^{\mathrm{PBE-SOC}}$), and similar band profiles with wider band gaps ($E_g^{\mathrm{HSE-SOC}}$) are obtained with hybrid functionals. All calculated band gaps together with the location of valence band maximum (VBM) and conduction band minimum (CBM) are summarized in Table IV.

TABLE IV. Energy band gaps at the level of GGA-PBE, E_g^{PBE}; GGA-PBE+SOC, $E_g^{\mathrm{PBE-SOC}}$; HSE06+SOC, $E_g^{\mathrm{HSE-SOC}}$; and the locations of VBM and CBM edges for 1H- and 1T'-WXO monolayers.

Crystal phase	E_g^{PBE} (eV)	$E_g^{\mathrm{PBE-SOC}}$ (eV)	$E_g^{\mathrm{HSE-SOC}}$ (eV)	VBM/CBM –
1H-WSO	1.52	1.48	2.06	Γ/K
1H-WSeO	1.28	1.23	1.78	Γ/K
1H-WTeO	0.71	0.52	0.97	Γ/Γ-M
1T'-WSO	SM	SM	SM	Γ- X/S -Y
1T'-WSeO	0.25	0.15	0.29	S -Y/Y
1T'-WTeO	0.41	0.25	0.61	Γ- S/S -Y

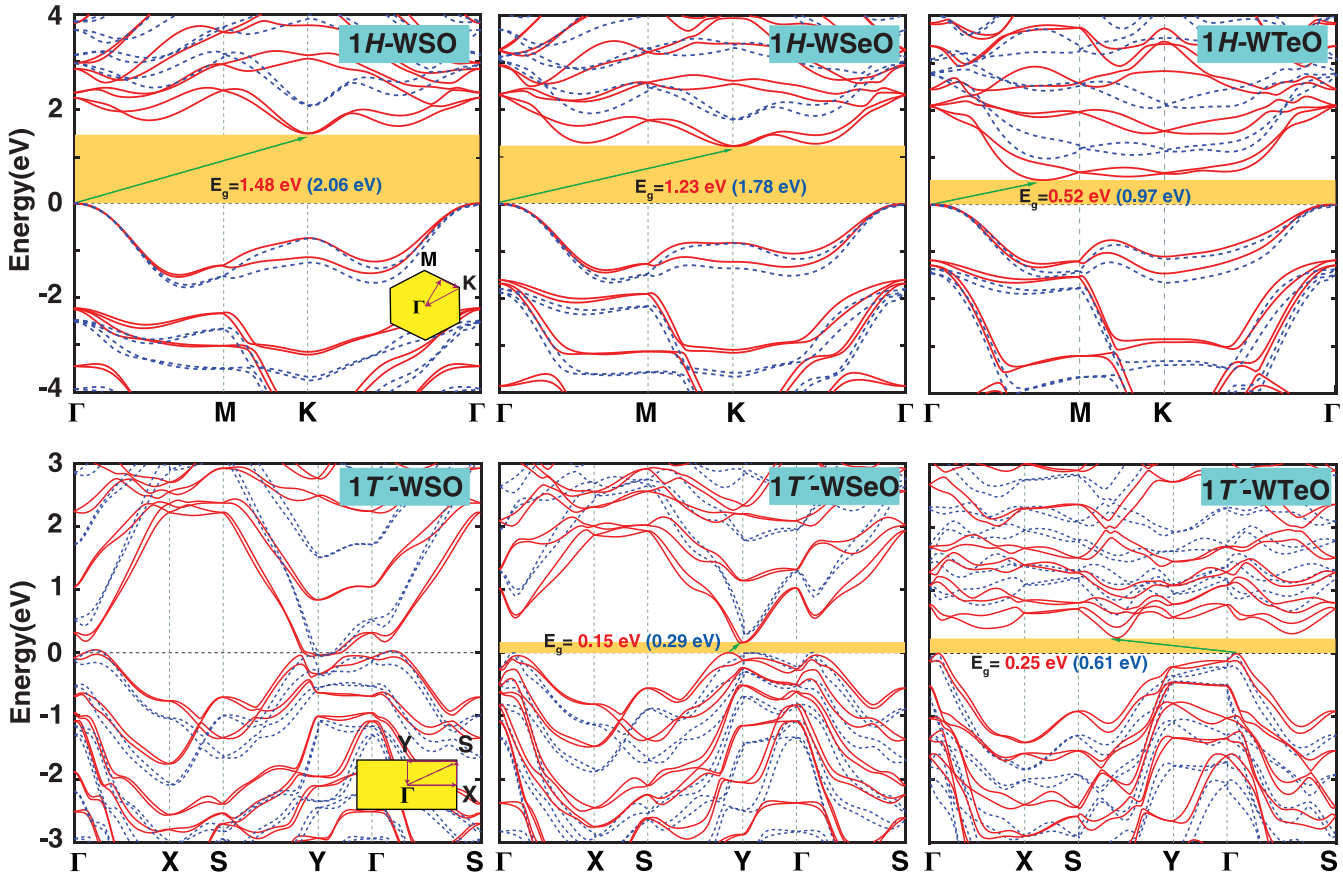

FIG. 5. The electronic band structures of Janus 1H- and 1T'-WXO monolayers. The results based on GGA-PBE+SOC and HSE06+SOC are shown by red solid and dashed blue lines, respectively. The band gap values at the level of PBE+SOC is shaded by light orange rectangles. $E_g^{\mathrm{PBE-SOC}}$ and $E_g^{\mathrm{HSE-SOC}}$ values are given. The Fermi level is set to zero.

IV. CONCLUSION

The stability and fundamental properties of 1H-, 1T-, and 1T' phases of Janus WXO (X = S, Se, and Te) monolayers were investigated. Our vibrational frequency analysis revealed that the 1T-WXO monolayers are prone to instability and transform to a 1T'-phase similar to their binary counterparts. On the other hand, 1H- and 1T'-WXO monolayers retain their crystalline structures up to 600 K. Raman spectrum analysis showed that the formation of Janus WXO monolayers results in new Raman active phonon modes (four for 1H and fifteen for 1T' phase) different from WX_2 systems. The heat capacity (C_V) of 1H- and 1T'-WXO monolayers varies with T^2 and $T^{1.75}$ for low-temperature ranges and expectedly converges to the classical limit as temperature increases. The mechanical properties of the 1H phase were found to be isotropic and the calculated in-plane stiffness values (C) are larger than the corresponding binary counterpart. Accordingly, the oxygenation makes the systems stiffer. On the other hand, the mechanical response of 1T'-WXO monolayers was calculated to be orientation dependent and the anisotropy along armchair and zigzag direction becomes more evident down the chalcogen group. The estimated Poisson's ratio range indicated that both phases are brittle. Following the calculation of elastic tensor elements, the piezoelectricity in 1H- and 1T'-WXO crystals was investigated, and large out-of-plane piezoelectric coefficients were shown to appear in both of phases due to the broken out-of-plane symmetry. It was obtained that while 1H-WX_2 monolayers have direct band gaps, 1H-WXO systems are indirect band-gap semiconductors and the band gap narrows down the chalcogen group. The direct to indirect transition is linked to the induced strain on X and O sides, and also correlated with the band-structure profile of 1H-WO_2. Except 1T'-WSO, 1T'-WSeO, and 1T'-WTeO are narrow band-gap semiconductors due to the Peierls distortion. The inclusion of SOC lowers the band gap for both phases, and the effect is found to be more distinct as X atoms get heavier. The versatile mechanical and electronic properties of Janus WXO monolayers together with their large piezoelectric response suggest that these systems are suitable materials for diverse applications.

ACKNOWLEDGMENTS

This work was supported by the Scientific and Technological Research Council of Turkey (TUBITAK) under Project No. 117F383. The calculations were performed at TUBITAK ULAKBIM, High Performance and Grid Computing Center (TR-Grid e-Infrastructure) and the National Center for High Performance Computing of Turkey (UHeM) under Grant No. 5007092019. M.Y. was supported by the Flemish Science Foundation (FWO-Vl) by a postdoctoral fellowship.

[1] K. S. Novoselov, A. K. Geim, S. V. Morozov, D. Jiang, Y. Zhang, S. V. Dubonos, I. V. Grigorieva, and A. A. Firsov, Science **306**, 666 (2004).

[2] J. Li, N. V. Medhekar, and V. B. Shenoy, J. Phys. Chem. C **117**, 15842 (2013).

[3] H. Guo, N. Lu, L. Wang, X. Wu, and X. C. Zeng, J. Phys. Chem. C **118**, 7242 (2014).

[4] G. Cunningham, M. Lotya, C. S. Cucinotta, S. Sanvito, S. D. Bergin, R. Menzel, M. S. Shaffer, and J. N. Coleman, ACS Nano **6**, 3468 (2012).

[5] C. Ataca, H. Sahin, and S. Ciraci, J. Phys. Chem. C **116**, 8983 (2012).

[6] K. F. Mak and J. Shan, Nat. Photon. **10**, 216 (2016).

[7] A. C. Neto and K. Novoselov, Rep. Prog. Phys. **74**, 082501 (2011).

[8] K. F. Mak, C. Lee, J. Hone, J. Shan, and T. F. Heinz, Phys. Rev. Lett. **105**, 136805 (2010).

[9] A. Splendiani, L. Sun, Y. Zhang, T. Li, J. Kim, C.-Y. Chim, G. Galli, and F. Wang, Nano Lett. **10**, 1271 (2010).

[10] J. Ye, Y. J. Zhang, R. Akashi, M. S. Bahramy, R. Arita, and Y. Iwasa, Science **338**, 1193 (2012).

[11] D. Costanzo, S. Jo, H. Berger, and A. F. Morpurgo, Nat. Nanotechnol. **11**, 339 (2016).

[12] Q. H. Wang, K. Kalantar-Zadeh, A. Kis, J. N. Coleman, and M. S. Strano, Nat. Nanotechnol. **7**, 699 (2012).

[13] M. Kan, J. Wang, X. Li, S. Zhang, Y. Li, Y. Kawazoe, Q. Sun, and P. Jena, J. Phys. Chem. C **118**, 1515 (2014).

[14] S. Kumar and U. Schwingenschlogl, Chem. Mater. **27**, 1278 (2015).

[15] C. Cong, J. Shang, X. Wu, B. Cao, N. Peimyoo, C. Qiu, L. Sun, and T. Yu, Adv. Opt. Mater. **2**, 131 (2014).

[16] Q. Fu, L. Yang, W. Wang, A. Han, J. Huang, P. Du, Z. Fan, J. Zhang, and B. Xiang, Adv. Mater. **27**, 4732 (2015).

[17] K.-A. N. Duerloo, Y. Li, and E. J. Reed, Nat. Commun. **5**, 4214 (2014).

[18] Y. Li, K.-A. N. Duerloo, K. Wauson, and E. J. Reed, Nat. Commun. **7**, 10671 (2016).

[19] P. Chen, W. W. Pai, Y.-H. Chan, W.-L. Sun, C.-Z. Xu, D.-S. Lin, M. Y. Chou, A.-V. Fedorov, and T.-C. Chiang, Nat. Commun. **9**, 2003 (2018).

[20] M. S. Sokolikova, P. C. Sherrell, P. Palczynski, V. L. Bemmer, and C. Mattevi, Nat. Commun. **10**, 712 (2019).

[21] H. R. Gutiérrez, N. Perea-López, A. L. Elías, A. Berkdemir, B. Wang, R. Lv, F. López-Urías, V. H. Crespi, H. Terrones, and M. Terrones, Nano Lett. **13**, 3447 (2013).

[22] N. Peimyoo, W. Yang, J. Shang, X. Shen, Y. Wang, and T. Yu, ACS Nano **8**, 11320 (2014).

[23] Z. Y. Zhu, Y. C. Cheng, and U. Schwingenschlögl, Phys. Rev. B **84**, 153402 (2011).

[24] H. Fang, S. Chuang, T. C. Chang, K. Takei, T. Takahashi, and A. Javey, Nano Lett. **12**, 3788 (2012).

[25] D. Yang, X. Fan, F. Zhang, Y. Hu, and Z. Luo, Nanoscale Res. Lett. **14**, 1 (2019).

[26] M. N. Ali, J. Xiong, S. Flynn, J. Tao, Q. D. Gibson, L. M. Schoop, T. Liang, N. Haldolaarachchige, M. Hirschberger, N. P. Ong *et al.*, Nature (London) **514**, 205 (2014).

[27] A. A. Soluyanov, D. Gresch, Z. Wang, Q. Wu, M. Troyer, X. Dai, and B. A. Bernevig, Nature (London) **527**, 495 (2015).

[28] K. V. Shanavas and S. Satpathy, Phys. Rev. B **91**, 235145 (2015).

[29] J. Liu, H. Liu, J. Wang, H. Sheng, G. Tang, J. Zhang, and D. Bai, Physica B: Condens. Matter. **568**, 18 (2019).

[30] Y. Ma, Y. Dai, M. Guo, C. Niu, J. Lu, and B. Huang, Phys. Chem. Chem. Phys. **13**, 15546 (2011).

[31] A.-Y. Lu, H. Zhu, J. Xiao, C.-P. Chuu, Y. Han, M.-H. Chiu, C.-C. Cheng, C.-W. Yang, K.-H. Wei, Y. Yang *et al.*, Nat. Nanotechnol. **12**, 744 (2017).

[32] J. Zhang, S. Jia, I. Kholmanov, L. Dong, D. Er, W. Chen, H. Guo, Z. Jin, V. B. Shenoy, L. Shi *et al.*, ACS Nano **11**, 8192 (2017).

[33] D. B. Trivedi, G. Turgut, Y. Qin, M. Y. Sayyad, D. Hajra, M. Howell, L. Liu, S. Yang, N. H. Patoary, H. Li *et al.*, Adv. Mater. **32**, 2006320 (2020).

[34] Y.-C. Lin, C. Liu, Y. Yu, E. Zarkadoula, M. Yoon, A. A. Puretzky, L. Liang, X. Kong, Y. Gu, A. Strasser *et al.*, ACS Nano **14**, 3896 (2020).

[35] R. Sant, M. Gay, A. Marty, S. Lisi, R. Harrabi, C. Vergnaud, M. T. Dau, X. Weng, J. Coraux, N. Gauthier *et al.*, npj 2D Mater. Appl. **4**, 41 (2020).

[36] L. Dong, J. Lou, and V. B. Shenoy, ACS Nano **11**, 8242 (2017).

[37] M. Yagmurcukardes, Y. Qin, S. Ozen, M. Sayyad, F. M. Peeters, S. Tongay, and H. Sahin, Appl. Phys. Rev. **7**, 011311 (2020).

[38] Z. Kahraman, A. Kandemir, M. Yagmurcukardes, and H. Sahin, J. Phys. Chem. C **123**, 4549 (2019).

[39] A. Mogulkoc, Y. Mogulkoc, S. Jahangirov, and E. Durgun, J. Phys. Chem. C **123**, 29922 (2019).

[40] M. Demirtas, M. J. Varjovi, M. M. Cicek, and E. Durgun, Phys. Rev. Materials **4**, 114003 (2020).

[41] M. Demirtas, B. Ozdemir, Y. Mogulkoc, and E. Durgun, Phys. Rev. B **101**, 075423 (2020).

[42] J. Wang, H. Shu, T. Zhao, P. Liang, N. Wang, D. Cao, and X. Chen, Phys. Chem. Chem. Phys. **20**, 18571 (2018).

[43] M. Yagmurcukardes, C. Sevik, and F. M. Peeters, Phys. Rev. B **100**, 045415 (2019).

[44] M. A. U. Absor, H. Kotaka, F. Ishii, and M. Saito, Jpn. J. Appl. Phys. **57**, 04FP01 (2018).

[45] Y. Sun, Z. Shuai, and D. Wang, Nanoscale **10**, 21629 (2018).

[46] M. Yagmurcukardes and F. M. Peeters, Phys. Rev. B **101**, 155205 (2020).

[47] F. A. Rasmussen and K. S. Thygesen, J. Phys. Chem. C **119**, 13169 (2015).

[48] A. P. Dral and E. Johan, Sens. Actuat. B **272**, 369 (2018).

[49] P. Kumbhakar, C. C. Gowda, P. L. Mahapatra, M. Mukherjee, K. D. Malviya, M. Chaker, A. Chandra, B. Lahiri, P. Ajayan, D. Jariwala *et al.*, Mater. Today (2021).

[50] K. Kalantar-zadeh, J. Z. Ou, T. Daeneke, A. Mitchell, T. Sasaki, and M. S. Fuhrer, Appl. Mater. Today **5**, 73 (2016).

[51] M. Kang, H. I. Yang, and W. Choi, J. Phys. D **52**, 505105 (2019).

[52] H. Shioya, K. Tsukagoshi, K. Ueno, and A. Oiwa, Jpn. J. Appl. Phys. **58**, 120903 (2019).

[53] H. Kim, J. Kim, S.-K. Kim, and S. H. Ahn, Appl. Catal. B **232**, 93 (2018).

[54] P. V. Sarma, T. V. Vineesh, R. Kumar, V. Sreepal, R. Prasannachandran, A. K. Singh, and M. M. Shaijumon, ACS Catal. **10**, 6753 (2020).

[55] W. Kohn and L. J. Sham, Phys. Rev. **140**, A1133 (1965).

[56] P. Hohenberg and W. Kohn, Phys. Rev. **136**, B864 (1964).

[57] G. Kresse and J. Hafner, Phys. Rev. B **47**, 558 (1993).

[58] G. Kresse and J. Hafner, Phys. Rev. B **49**, 14251 (1994).

[59] G. Kresse and J. Furthmüller, Comput. Mater. Sci. **6**, 15 (1996).

[60] G. Kresse and J. Furthmüller, Phys. Rev. B **54**, 11169 (1996).

[61] P. E. Blöchl, Phys. Rev. B **50**, 17953 (1994).

[62] J. P. Perdew, K. Burke, and M. Ernzerhof, Phys. Rev. Lett. **77**, 3865 (1996).

[63] J. Heyd, G. E. Scuseria, and M. Ernzerhof, J. Chem. Phys. **118**, 8207 (2003).

[64] A. V. Krukau, O. A. Vydrov, A. F. Izmaylov, and G. E. Scuseria, J. Chem. Phys. **125**, 224106 (2006).

[65] H. J. Monkhorst and J. D. Pack, Phys. Rev. B **13**, 5188 (1976).

[66] A. Togo and I. Tanaka, Scr. Mater. **108**, 1 (2015).

[67] M. Yagmurcukardes, F. M. Peeters, and H. Sahin, Phys. Rev. B **98**, 085431 (2018).

[68] G. Henkelman, A. Arnaldsson, and H. Jónsson, Comput. Mater. Sci. **36**, 354 (2006).

[69] See Supplemental Material at http://link.aps.org/supplemental/10.1103/PhysRevB.103.195438 for additional details on structural and electronic properties of WX_2 monolayers, molecular dynamics results, and project density states analysis of Janus W*X*O systems.

[70] J. Reyes-Retana and F. Cervantes-Sodi, Sci. Rep. **6**, 24093 (2016).

[71] F. Ersan, S. Cahangirov, G. Gökoğlu, A. Rubio, and E. Aktürk, Phys. Rev. B **94**, 155415 (2016).

[72] S. Tongay, H. Sahin, C. Ko, A. Luce, W. Fan, K. Liu, J. Zhou, Y.-S. Huang, C.-H. Ho, J. Yan *et al.*, Nat. Commun. **5**, 3252 (2014).

[73] M. Calandra, Phys. Rev. B **88**, 245428 (2013).

[74] Y.-J. Zhang, R.-N. Wang, G.-Y. Dong, S.-F. Wang, G.-S. Fu, and J.-L. Wang, AIP Adv. **9**, 125208 (2019).

[75] N. Lu, C. Zhang, C.-H. Lee, J. P. Oviedo, M. A. T. Nguyen, X. Peng, R. M. Wallace, T. E. Mallouk, J. A. Robinson, J. Wang *et al.*, J. Phys. Chem. C **120**, 8364 (2016).

[76] Q.-L. Xiong, J. Zhou, J. Zhang, T. Kitamura, and Z.-H. Li, Phys. Chem. Chem. Phys. **20**, 20988 (2018).

[77] M. Neek-Amal, J. Beheshtian, F. Shayeganfar, S. K. Singh, J. H. Los, and F. M. Peeters, Phys. Rev. B **87**, 075448 (2013).

[78] M. M. Petrić, M. Kremser, M. Barbone, Y. Qin, Y. Sayyad, Y. Shen, S. Tongay, J. J. Finley, A. R. Botello-Méndez, and K. Müller, Phys. Rev. B **103**, 035414 (2021).

[79] H. Sahin, Phys. Rev. B **92**, 085421 (2015).

[80] A. A. Balandin, Nat. Mater. **10**, 569 (2011).

[81] G. Qin, Z. Qin, H. Wang, and M. Hu, Phys. Rev. B **95**, 195416 (2017).

[82] Y. Wang, J. Xiao, H. Zhu, Y. Li, Y. Alsaid, K. Y. Fong, Y. Zhou, S. Wang, W. Shi, Y. Wang *et al.*, Nature (London) **550**, 487 (2017).

[83] W. Shi and Z. Wang, J. Phys.: Condens. Matter **30**, 215301 (2018).

[84] R. M. Christensen, *The Theory of Materials Failure* (Oxford University Press, Oxford, 2013).

[85] S.-E. Park and T. R. Shrout, J. Appl. Phys. **82**, 1804 (1997).

[86] T. Wu and H. Zhang, Angew. Chem. Int. Ed. **54**, 4432 (2015).

[87] M. N. Blonsky, H. L. Zhuang, A. K. Singh, and R. G. Hennig, ACS Nano **9**, 9885 (2015).

[88] R. Englman, *The Jahn-Teller Effect in Molecules and Crystals* (Wiley-Interscience, New York, 1972).

[89] X. Zhou, H. Shu, Q. Li, P. Liang, D. Cao, and X. Chen, J. Mater. Chem. C **8**, 4432 (2020).